JBC RESEARCH ARTICLE

The molecular principles underlying diverse functions of the SLC26 family of proteins

Received for publication, January 27, 2024, and in revised form, March 7, 2024 Published, Papers in Press, April 4, 2024,
https://doi.org/10.1016/j.jbc.2024.107261

Satoe Takahashi[1,2] **and Kazuaki Homma**[1,2,3,*]

From the [1]*Department of Otolaryngology – Head and Neck Surgery, Feinberg School of Medicine, Northwestern University, Chicago, Illinois, USA;* [2]*Center for Mechanical Excitability, The University of Chicago, Chicago, Illinois, USA;* [3]*The Hugh Knowles Center for Clinical and Basic Science in Hearing and Its Disorders, Northwestern University, Evanston, Illinois, USA*

Reviewed by members of the JBC Editorial Board. Edited by Mike Shipston

Mammalian SLC26 proteins are membrane-based anion transporters that belong to the large SLC26/SulP family, and many of their variants are associated with hereditary diseases. Recent structural studies revealed a strikingly similar homodimeric molecular architecture for several SLC26 members, implying a shared molecular principle. Now a new question emerges as to how these structurally similar proteins execute diverse physiological functions. In this study, we sought to identify the common *versus* distinct molecular mechanism among the SLC26 proteins using both naturally occurring and artificial missense changes introduced to SLC26A4, SLC26A5, and SLC26A9. We found: (i) the basic residue at the anion binding site is essential for both anion antiport of SLC26A4 and motor functions of SLC26A5, and its conversion to a nonpolar residue is crucial but not sufficient for the fast uncoupled anion transport in SLC26A9; (ii) the conserved polar residues in the N- and C-terminal cytosolic domains are likely involved in dynamic hydrogen-bonding networks and are essential for anion antiport of SLC26A4 but not for motor (SLC26A5) and uncoupled anion transport (SLC26A9) functions; (iii) the hydrophobic interaction between each protomer's last transmembrane helices, TM14, is not of functional significance in SLC26A9 but crucial for the functions of SLC26A4 and SLC26A5, likely contributing to optimally orient the axis of the relative movements of the core domain with respect to the gate domains within the cell membrane. These findings advance our understanding of the molecular mechanisms underlying the diverse physiological roles of the SLC26 family of proteins.

The solute carrier 26 (SLC26)/sulfate permease (SulP) proteins constitute a large gene family, many of which function as solute transporters (1). Increasing number of genetic variants are associated with various human diseases such as nephrocalcinosis (SLC26A1), hyperoxalemia (SLC26A1), diastrophic dysplasia (SLC26A2), achondrogenesis (SLC26A2), atelosteogenesis (SLC26A2), multiple epiphyseal dysplasia (SLC26A2), congenital chloride diarrhea (SLC26A3), deafness (SLC26A4 and SLC26A5), bicarbonate metabolism-related diseases (SLC26A6), hypothyroidism (SLC26A7), asthenozoospermia (SLC26A8), bronchiectasis (SLC26A9), and dysregulation of chloride homeostasis and neuroactivity (SLC26A11) (1–3). The amino acid sequences among the SLC26 family members are quite similar, and recent structural studies revealed that their overall molecular architectures are also similar for mammalian SLC26A4 (4, 5), SLC26A5 (6–9), SLC26A6 (10), and SLC26A9 (11, 12). Thus, it is conceivable that a common molecular mechanism underlies their diverse physiological roles, and the pathogenic variants found in one SLC26 protein may affect the functions of the other family members in similar manners. However, it is not clear how SLC26 family members with similar structures can support their diverse physiological functions. It is possible that certain molecular features are not shared among family members, and thus some variants are pathogenic only in a certain family member(s) but not in others. In this study, we sought to understand the common *versus* distinct molecular mechanisms of the SLC26 proteins. To this end, we focus on three mammalian SLC26 family members with highly distinct functionalities, SLC26A4, SLC26A5, and SLC26A9. SLC26A4 (pendrin) is an electroneutral coupled anion exchanger that is essential for normal inner ear function (13–17). SLC26A5 (prestin) is a voltage-driven motor protein responsible for cochlear amplification and thus essential for normal hearing (18–22). SLC26A5 also reportedly retains small anion exchanging function (23) but with minimal physiological significance (24). SLC26A9 mediates coupled or uncoupled anion transport (12, 25–28). The uncoupled chloride transport is rapid and shows discrete channel-like unitary conductance (28). SLC26A9 plays crucial roles in gastric acid secretion (29) and airway clearance (30). The roles of SLC26A9 in renal chloride excretion and arterial pressure regulation are also reported (31), despite its low expression in the kidney (25, 28).

We examined the functional consequences of various missense changes introduced to these three SLC26 proteins. We found that (i) the basic residues at the anion substrate binding site are crucial for the anion antiport and voltage-dependent motor functions of SLC26A4 and SLC26A5, respectively, whereas nonpolar residue at the equivalent site is crucial but not sufficient for rapid uncoupled electrogenic anion transport in SLC26A9, that (ii) conserved polar residues

* For correspondence: Kazuaki Homma, k-homma@northwestern.edu.

at the interface between the N- and C-terminal cytosolic domains likely contribute to form dynamic hydrogen-bonding networks and are crucial for the functions of SLC26A4, but not for SLC26A5 and SLC26A9, and that (iii) the hydrophobic interaction at the dimerization interface at the C-terminal ends of the last transmembrane helix, TM14, is not of functional importance for uncoupled anion transport in SLC26A9 but essential for the anion antiport and motor functions of SLC26A4 and SLC26A5, respectively. This comparative functional study thus provides mechanistic insights underlying the diverse physiological functions of the SLC26 family of proteins, which refines the accuracy of our pathogenicity assessment of disease-associated variants in this important family of proteins.

Results

SLC26 constructs generated in this study

Recent single particle cryo-EM studies have revealed homodimeric structures for mammalian SLC26A4 (4, 5) (Fig. 1*A*, left), SLC26A5 (6–9) (Fig. 1*A*, middle), SLC26A6 (10), and SLC26A9 (11, 12) (Fig. 1*A*, right). The N- and C-termini physically interact to one another to form the cytoplasmic domain (CD), and the intervening sequence constitutes the transmembrane domain (TMD). TMD is comprised of 14 transmembrane helices (TM1-14) that are divided into the core (TM1-4, TM8-11) and gate (TM5-7, TM12-14) subdomains. Each SLC26 protomer has its anion-binding pocket and anion translocation pathway between these two TMD subdomains. Basic residues are found at the anion-binding site except for SLC26A9 (Fig. 1*B*). Elevator-like up and down movements of the core domain with respect to the gate domain underlie the anion transport functions and are also thought to account for the motor function of SLC26A5 (32). Homodimerization appears to be essential for rigidly maintaining the axis of the elevator-like core domain movements perpendicular to the cell membrane plane. Two hydrophobic residues at the C-terminus of TM14 are conserved (Fig. 1*B*) and seem to contribute to homodimerization. They also seem to be crucial for determining and maintaining the orientation of the gate domains within the cell membrane (Fig. 1, *A* and *C*). The N- and C-termini are interwound, and their interaction is likely stabilized by the hydrogen bond (H-bond) networks (Fig. 1, *A* and *C*). Although conformational changes at these N- and C-terminal interaction sites are subtle (4, 6, 7), it is conceivable that the H-bond networks are dynamic and intimately linked to large conformational changes in TMD (Figs. 1*D* and S1), possibly contributing to interprotomer functional communications.

The functional importance of these key regions of interest is implied by the presence of multiple disease-associated *SLC26A4* missense variants identified in humans (Fig. 1*A*, left). Hence, we systematically examined the functional consequences of the following missense changes, aiming at gaining mechanistic insights underlying the diverse functions of the SLC26 proteins, Y20H, V509G, V510D, V510I, H723D, and H723Y in SLC26A4; Y16H, R399V, I500V, and H707R in SLC26A5; Y8H, V393R, V493G, and H731R in SLC26A9. Among these, Y20H (c.58T>C), V510D (c.1529T>A), H723D (c.2167C>G), and H723Y (c.2167C>T), were identified in *SLC26A4* in human patients (33–36), while the others are not. All SLC26 constructs including wild-type (WT) controls were C-terminally tagged with mTurquoise2 (mTq2) and expressed in HEK293T cells in a doxycycline (Dox)-inducible manner for functional assays as in previous studies (37, 38). To quantitatively assess membrane targeting, HEK293T cells heterologously expressing WT and mutated SLC26 proteins were treated with membrane impermeable sulfo-Cyanine3 (Cy3) NHS ester that labeled proteins expressed in the plasma membrane. The cells were subsequently lysed in a solution containing a mild detergent, and the solubilized SLC26 proteins were immunoprecipitated using nanobody that recognizes mTq2. The ratios of Cy3 and mTq2 fluorescence on beads, F_{Cy3}/F_{mTq2}, indicate the membrane targeting efficiencies of the SLC26 constructs (9). HEK293T cells expressing only the mTq2 moiety were used as negative control. The F_{Cy3}/F_{mTq2} ratios were normalized to WT controls and summarized in Figure 2. We found that the F_{Cy3}/F_{mTq2} ratios of all SLC26 constructs were higher than those of the negative controls (mTq2 alone), affirming that none of the missense changes introduced abrogated the membrane targeting of the SLC26 proteins. The relative F_{Cy3}/F_{mTq2} ratios (Fig. 2) were used for correcting the measured anion transport activities of SLC26A4 and SLC26A9 (see below).

The anion-binding site

Basic residues at the N-terminus of TM10 in the core domain (Fig. 1, *A* and *B*) likely contribute to transiently attract and hold anion substrates during the transport process. The importance of this highly conserved basic residue in SLC26A4 (Arg^{409}) is reflected by the presence of multiple disease-associated missense variants, that is, R409C (c.1225C>T) (39), R409H (c.1226G>A) (40), R409L (c.1226G>T) (41), and R409P (c.1226G>C) (42), and has been experimentally demonstrated (38, 43–47). In SLC26A6, Arg^{404} is experimentally demonstrated to be important for its anion antiport function (10). Interestingly, SLC26A9, which mediates channel-like fast uncoupled electrogenic chloride transport (26–28), has a nonpolar residue, Val^{393}, at the equivalent position (Fig. 1*B*). To examine the functional importance of Val^{393} in SLC26A9, we measured whole-cell currents in HEK293T cells expressing WT and V393R SLC26A9 (hA9-WT and hA9-V393R, respectively, in Fig. 3). Cells not treated with Dox (negative control) showed very small chloride current as expected, whereas those expressing WT (hA9-WT) showed very large currents (the whole-cell currents were corrected for cell size) (Fig. 3*A*). In some cells, the hA9-WT-mediated chloride conductance was so high that the measured whole-cell currents were limited by the series resistance of the recording pipette. Thus, the mean magnitude of the chloride conductance density shown in Figure 3*B* for hA9-WT is underestimated to an unknown degree (indicated by an upward arrow). Conversion of Val^{393} to Arg (hA9-V393R) resulted in very small conductance density that was statistically

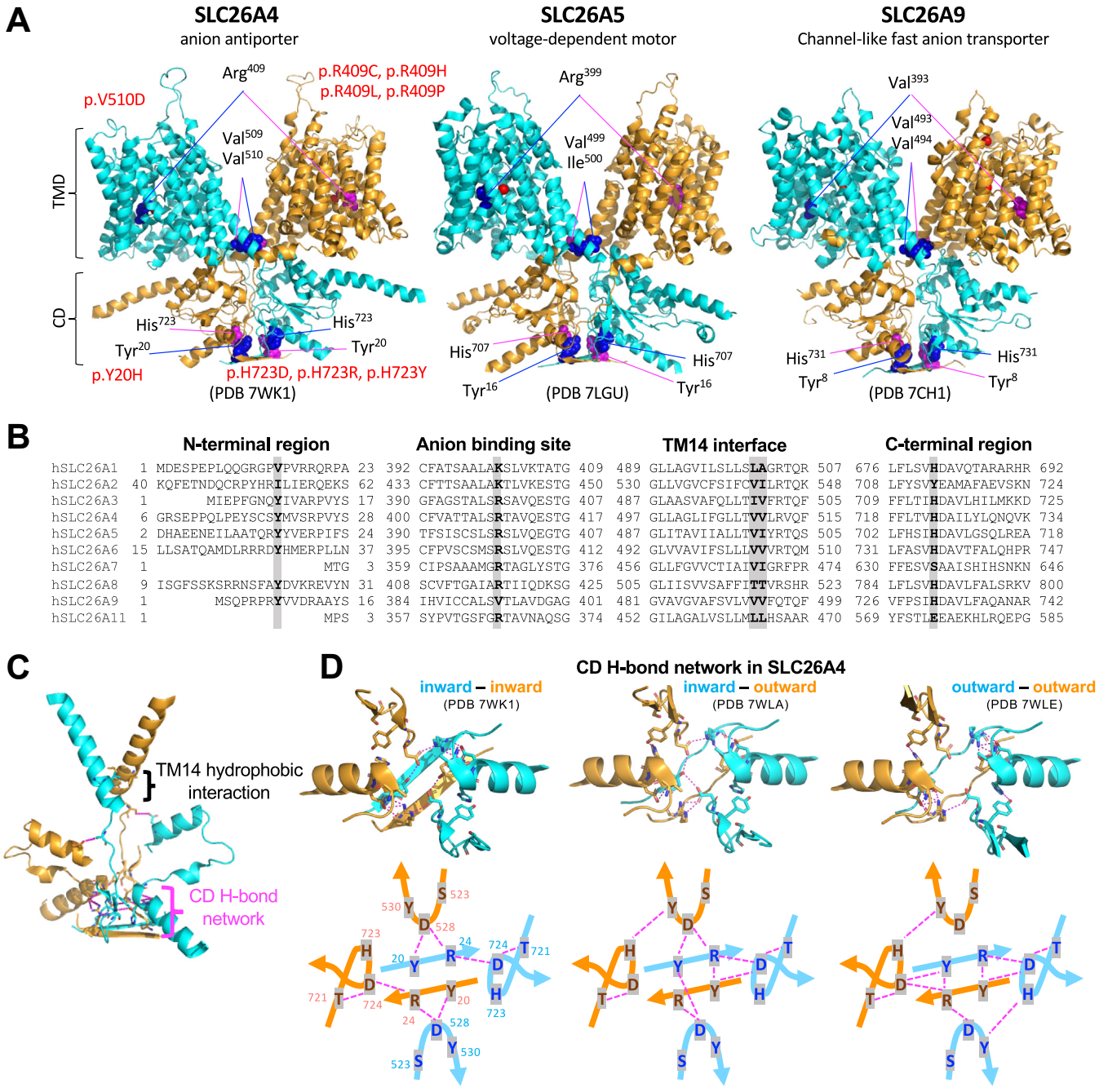

Figure 1. The amino acid residues of interest in this study. *A*, the cryo-EM homodimeric structures of mouse SLC26A4 (*left*), human SLC26A5 (*middle*), and human SLC26A9 (*right*). The locations of the amino acid residues of interest in this study are shown in sphere representation in *blue* (in one protomer shown in *cyan*) and *magenta* (in the other protomer shown in *orange*). Missense variants shown in *red* were identified in *SLC26A4* in human patients. TMD, transmembrane domain; CD, cytoplasmic domain. *B*, amino acid sequence comparison among human SLC26 proteins for selected protein regions. The amino acid residues of interest in this study are indicated in bold and highlighted. The residue numbers at the N- and C-termini are also shown. *C*, TM14 helices and selected C-terminal structures in mouse SLC26A4 (PDB: 7WK1). Tyr^{20}, Arg^{24}, Val^{509}, Val^{510}, Ser^{517}, Ser^{523}, Asp^{528}, Tyr^{530}, Asp^{698}, Thr^{721}, His^{723}, and Asp^{724} are shown in stick representation. Magenta dashed lines (seen more easily in panel D) indicate potential hydrogen bond interactions. *D*, the N- and C-terminal interaction in mouse SLC26A4 in three distinct structural modes as indicated. Tyr^{20}, Arg^{24}, Ser^{523}, Asp^{528}, Tyr^{530}, Thr^{721}, His^{723}, and Asp^{724} are shown in stick representation. *Magenta* dashed lines indicate potential hydrogen bond interactions, which are schematically shown in lower panels for clarity.

indistinguishable from that of non-induced negative control (Fig. 3, *A* and *B*). As expected, chloride conductance density was also small and indistinguishable from non-induced negative control in cells expressing SLC26A5 (mA5-WT, Fig. 3, *A* and *B*). Interestingly, conversion of Arg^{399} to Val in SLC26A5 (mA5-R399V, Fig. 3*B*) slightly increased the mean conductance density although this increase was not statistically significant. We repeated whole-cell voltage clamp recordings using a low chloride-containing intracellular solution and determined the reversal potentials, E_{rev}, that are V_m readings at zero current and are independent of the series resistance (thus are immune to uncertainty introduced by correction for the

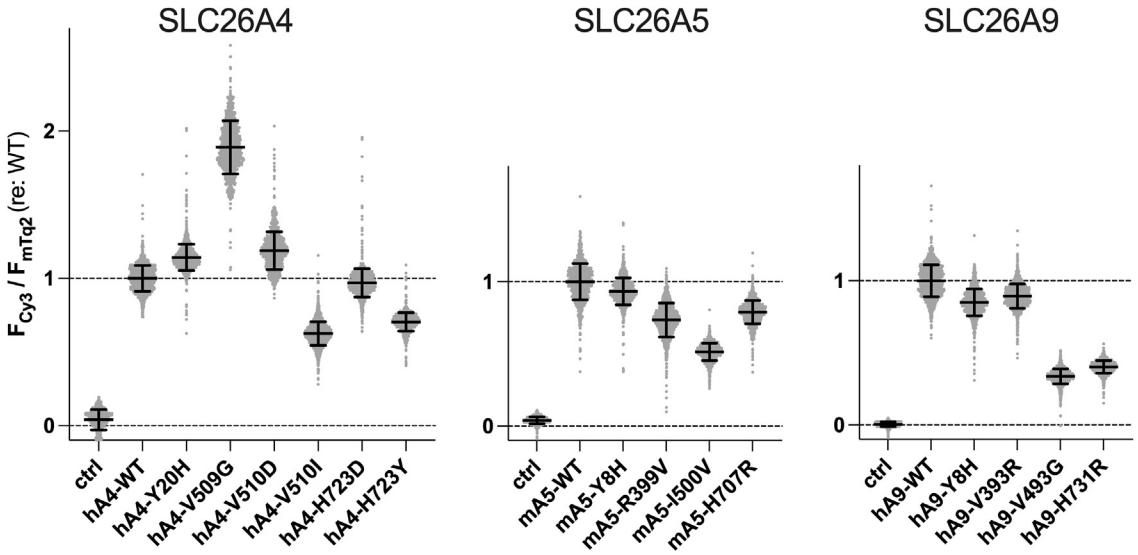

Figure 2. The membrane targeting efficiencies of the SLC26 constructs. HEK293T cells expressing various mTurquoise2 (mTq2)-tagged SLC26 proteins (hA4, human SLC26A4; mA5, mouse SLC26A5; and hA9, human SLC26A9) were treated with a membrane impermeable sulfo-Cy3 NHS ester to only label cell surface proteins. After lysing cells, mTq2-tagged SLC26 proteins were collected regardless of their original subcellular localizations using affinity beads that capture mTq2, and the ratios of Cy3 and mTq2 fluorescence, F_{Cy3}/F_{mTq2}, were determined and compared to those of WTs. The results were normalized to the WTs. Error bars indicate propagated errors computed using the standard deviations of the F_{Cy3}/F_{mTq2} data. HEK293T cells expressing only the mTq2 moiety were used as negative control (ctrl).

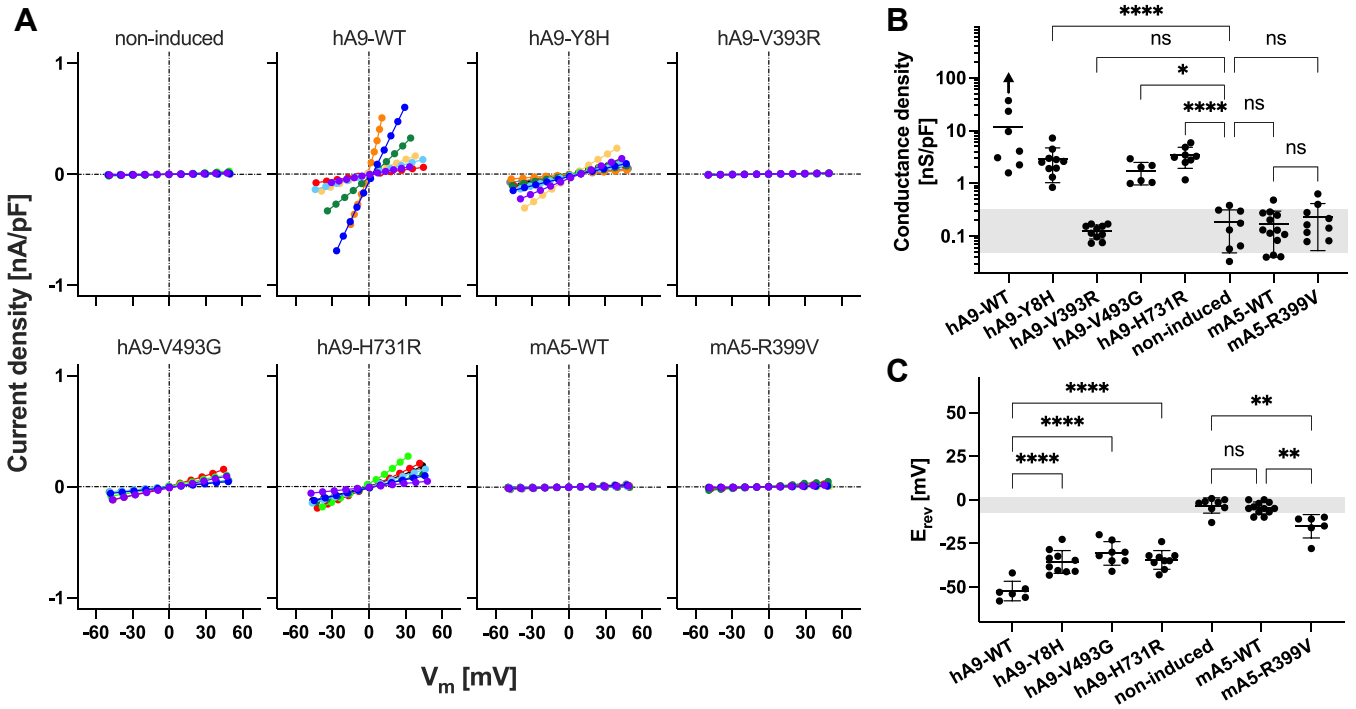

Figure 3. Whole-cell electrophysiological chloride transport assays. *A*, whole-cell conductance was recorded in HEK293T cells expressing various SLC26A9 and SLC26A5 proteins. The current-voltage data were corrected for the series resistance and divided by the cell membrane capacitance. Different colors indicate individual recordings. *B*, summaries of the whole-cell recordings. An upward arrow indicates an underestimation of the mean conductance density for hA9-WT (see the main text). Error bars indicate standard deviations. A gray shade indicates the mean ± standard deviation of the non-induced negative control. *C*, summaries of reversal potentials (E_{rev}) determined using a low chloride-containing intracellular solution. Error bars indicate standard deviation. A gray shade indicates the mean ± standard deviation of the non-induced negative control. In panels (*B*) and (*C*), one-way ANOVA followed by Tukey's post hoc test was performed. "ns", $p \geq 0.05$. "*", $0.01 \leq p < 0.05$. "**", $0.001 \leq p < 0.01$. "***", $0.0001 \leq p < 0.001$. "****", $p < 0.0001$. In panel (*B*), the Kruskal-Wallis test followed by Dunn's multiple comparison test was also performed. This nonparametric analysis did not change the statistical conclusion except for "non-induced" *versus* "hA9-V493G" (not significant in the nonparametric test). The detailed statistics are provided in the supplementary data sheet.

series resistance). As expected, cells expressing hA9-WT showed greatly hyperpolarized E_{rev} due to the large chloride conductance and the large inward transmembrane chloride gradient ($[Cl^-]_{out}$ = 148 mM, $[Cl^-]_{in}$ = 10 mM) (Fig. 3*C*). Slightly hyperpolarized E_{rev} with statistical significance was found in cells expressing mA5-R399V, suggesting that the elimination of the basic residue from the anion binding site conferred small uncoupled chloride transport function on SLC26A5. This observation is in line with a recent report that R404V conferred a small, uncoupled chloride transport function on SLC26A6 (10).

The whole-cell electrophysiological assay (Fig. 3) has an advantage in directly assessing the channel-like function of SLC26A9 and its mutants using the physiologically relevant anion substrate, chloride. However, it does not inform if a change in the measured conductance is due to a change in the function of the SLC26A9 protein or an augmented/impaired membrane targeting. Distinguishing these possibilities is crucial, as the purpose of this study is to gain mechanistic insights into how structurally similar SLC26 proteins exert distinct functions. Since SLC26A9 also mediates iodide transport (26, 27), we further examined the transport function of WT and V399R SLC26A9 using iodide-sensitive mVenus$^{H148Q/I152L}$ that was coexpressed with the SLC26A9 constructs (Fig. 4*A*). As described in detail in our preceding study (38), this plate reader-based automated fluorometric assay using a large number of cells per well also determined total expression of mTq2-tagged protein (F_{mTq2}) and total cell density (OD_{660nm}) for each experiment (Fig. 4*B*). Combined with the membrane targeting efficiencies determined using sulfo-Cy3 NHS (Fig. 2, right panel), these extra measurements allowed determination of the amounts of mTq2-tagged SLC26

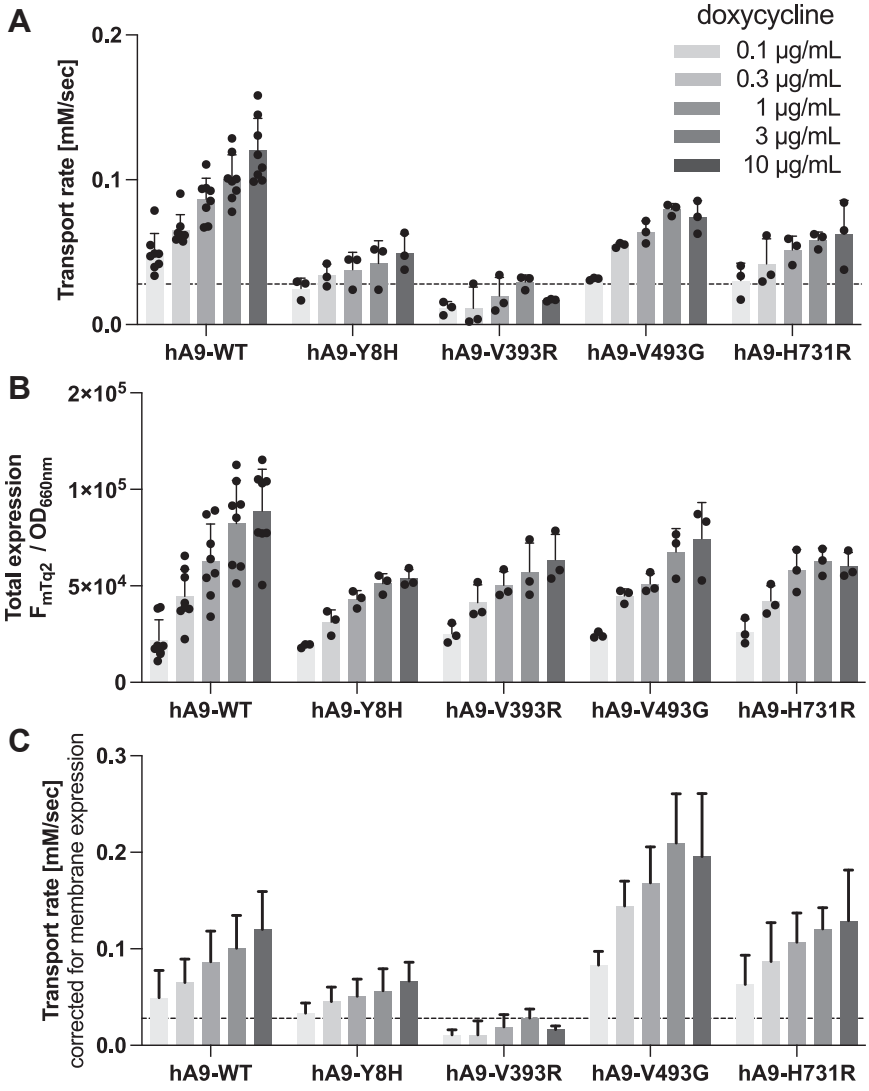

Figure 4. Multi-cell fluorometric iodide transport assays. *A*, iodide transport rates measured in HEK293T cells expressing various SLC26A9 constructs in a Dox-dependent manner. A horizontal dashed line indicates the basal iodide influx rate of non-induced cells (negative control). Error bars indicate standard deviation. *B*, ratios of mTq2 fluorescence (F_{mTq2}) and the optical densities (OD_{660nm}) of the cells expressing the mTq2-tagged SLC26A9 constructs, which quantify the total expressions of the SLC26A9 constructs. Error bars indicate standard deviation. *C*, SLC26A9-mediated iodide transport rates corrected for the relative membrane expressions. Error bars indicate propagated errors computed from the standard deviations in panel A and the errors in the relative membrane expressions.

constructs expressed in the cell membrane, for which the measured iodide transport rates were corrected. Specifically, we normalized the total expressions (F_{mTq2}/OD_{660nm}, Fig. 4*B*) to those of WT controls at each Dox dosage condition (resulting in WT values being one at all Dox conditions). These normalized total expression values were then multiplied by the membrane targeting efficiencies that were also normalized to WT controls (F_{Cy3}/F_{mTq2}, Fig. 2, right panel) to compute relative membrane expressions (F_{Cy3}/OD_{660nm}, "Fig. 4*B* re WT" in a supplementary data sheet). Finally, the Dox-dependent anion transport activities (Fig. 4*A*) were divided by these F_{Cy3}/OD_{660nm} values for correction of the membrane expressions (Fig. 4*C*, see also "Fig. 4*C*" in a supplementary data sheet). As expected, cells expressing hA9-WT showed Dox-dependent increase in iodide transport activity, whereas those expressing hA9-V393R did not, further demonstrating the essentiality of Val^{393} for the anion transport function of SLC26A9.

Although the anion transport by mammalian SLC26A5 is of minimal physiological significance (24), anions are still needed by SLC26A5 as extrinsic cofactors for supporting the fast motor function (48, 49, 50)). Arg^{399} very likely contributes to anion binding in SLC26A5, and its functional importance was experimentally demonstrated (51, 52). In line with these preceding studies, we found that HEK293T cells expressing R399V SLC26A5 (mA5-R399V) do not exhibit nonlinear capacitance (NLC, see Experimental procedures), which is the electrical signature of the voltage-driven motor function (electromotility) of SLC26A5 (Fig. 5*A*, top right), despite only a small negative effect of R399V on membrane targeting (Fig. 2,

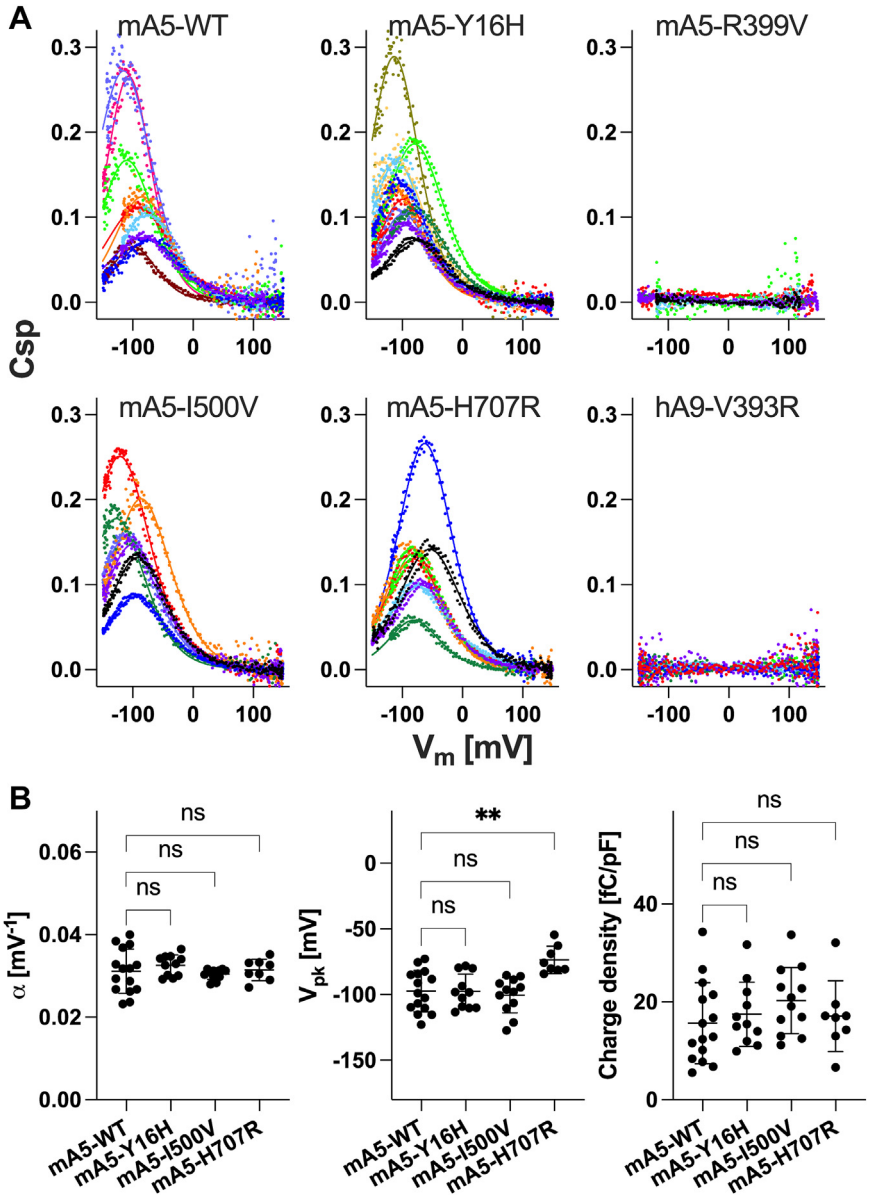

Figure 5. Whole-cell NLC recordings. *A*, representative NLC data. The magnitudes of NLC (C_m–C_{lin}) were corrected for cell size (C_{lin}), *i.e.*, $C_{sp} \equiv (C_m–C_{lin})/C_{lin}$. Different colors indicate individual recordings. A two-state Boltzmann model was used to interpret the NLC data (*solid lines*). *B*, summaries of the NLC parameters. One-way ANOVA combined with Tukey's post hoc test was performed. "ns", $p \geq 0.05$. "**", $0.001 \leq p < 0.01$.

middle panel). We also found that conversion of Val^{393} to Arg does not confer NLC on SLC26A9 (hA9-V393R), at least in the experimentally testable voltage range (Fig. 5*A*, bottom right). Note that NLC measurement was not feasible in cells expressing hA9-WT due to excessively high membrane conductance.

N- and C-terminal interactions in the cytosolic domains

H723R (c.2168A>G) is one of the most frequently found *SLC26A4* variants in patients, and preceding functional studies demonstrated that this common missense variant is dysfunctional (38, 46, 53–56). Multiple other disease-associated missense variants affecting His^{723} in SLC26A4 have also been reported (35, 36, 40), suggesting the importance of this His residue that is conserved among most SLC26 proteins (Fig. 1*B*). In the tertiary structure, this His residue is positioned very close to a Tyr residue at the N-terminus (Tyr^{20} in SLC26A4) (Fig. 1). Intriguingly, a disease-associated *SLC26A4* missense variant affecting this Tyr residue, Y20H (c.58T>C), was also reported (33). The cryo-EM structures of SLC26A4, A5, A6, and A9 point to the possibility that these conserved His and Tyr residues may be involved in H-bond networks at the bottom of CD where the N-termini interact with C-termini (Figs. 1, *C* and *D*, and S1). It is conceivable that these potential H-bond formations is dynamic and linked to the elevator-like large movements of the core domain to which the N-terminus is connected. Other residues that likely contribute to these H-bond networks are also conserved, and multiple *SLC26A4* missense variants affecting these residues have been reported to date, that is, R24G (c.70C>G), R24L (c.71G>T), R24Q (c.71G>A), Y530H (c.1588T>C), Y530S (c.1589A>C), T721K (c.2162C>A), T721M (c.2162C>T), D724G (c.2171A>G), D724N (c.2170G>A), and D724V (c.2171A>T) (33, 57–64). Among these variants, severe functional effects were demonstrated for Y530H, Y530S, T721M, and D724G (38, 54, 65, 66).

Using the SNARF-based fluorometric bicarbonate/chloride antiport assay that was established in our previous study (38) with subsequent correction for protein expression in the cell membrane as was done for the iodide transport assay in Figure 4 (see "Fig. 6*B* re WT" and "Fig. 6*C*" in the supplementary data sheet), we found that H723D and H723Y severely impaired the function of SLC26A4 (Fig. 6), similar to the common H723R. Y20H also resulted in the reduction of SLC26A4 antiport activity (Fig. 6). However, equivalent missense mutations only partially or barely affected the functions of SLC26A5 and SLC26A9. Specifically, Y16H did not alter the voltage sensitivity (α), voltage operating point (V_{pk}), and charge density of SLC26A5 (Fig. 5*A*, top middle, and Fig. 5*B*). H707R slightly shifted V_{pk} of SLC26A5, but α and charge density remained WT-like (Fig. 5*A* bottom middle, and Fig. 5*B*). Y8H reduced the anion transport activity of SLC26A9 (Figs. 3 and 4), but its negative functional impacts were relatively milder compared to that of Y20H in SLC26A4 (Fig. 6). Finally, the impact of H731R on the anion transport activity of SLC26A9 was very small (Figs. 3 and 4), which was in stark contrast to the severe functional effect of H723R in SLC26A4 (Fig. 6).

The homodimerization interface at the C-terminus of TM14

V499G is one of the artificial missense changes introduced to the junction between the TMD and the CD in SLC26A5 (67). This mutation does not impair the membrane targeting of SLC26A5 but virtually eradicates the motor function of SLC26A5 within the physiologically relevant voltage range (22, 68). The cryo-EM structures of SLC26A5 revealed that Val^{499} and Ile^{500} are at the homodimerization interface at the C-termini of TM14 helices (6–9) (Fig. 1), implying the importance of these hydrophobic residues for stabilizing the homodimeric structure. To examine the general functional importance of the hydrophobic interaction between TM14 helices, we introduced V509G and V493G mutations to SLC26A4 and SLC26A9, respectively, which are equivalent to V499G in SLC26A5. We found that V509G completely abolishes the anion transport function of SLC26A4 (Fig. 6), whereas V493G only partially or barely affected chloride and iodide transport, respectively, in SLC26A9 (Figs. 3 and 4). In the fluorometric iodide transport assay, influx of iodide was coupled to efflux of chloride to maintain electroneutrality, and this opposing anion fluxes is likely mediated by SLC26A9. Thus, the unabolished transport activity of hA9-V493G suggests that this missense change barely affects the coupled anion transport by SLC26A9.

Like V499G, I500G was also shown to abolish the motor function of SLC26A5 (9). Val^{510} in SLC26A4 is equivalent to Ile^{500} in SLC26A5, and a disease-associated missense change, V510D (c.1529T>A), has been reported (34). We found that this missense change also severely impairs the anion transport function of SLC26A4 (Fig. 6). The Val *versus* Ile difference is trivial if any for SLC26A5's motor function because I500V did not affect α, V_{pk}, and charge density of SLC26A5 (Fig. 5*A*, bottom left, and Fig. 5*B*). Interestingly, however, V510I in SLC26A4 largely reduced its anion transport function, although not to the same degree as V510D (Fig. 6).

Collectively, these observations imply the importance of the conserved hydrophobic residues at the C-termini of TM14 helices for fixing or confining the angles of the gate domains within a very small variable range in the cell membrane so that relative motions of the core domains with respect to the gate domains can complete alternating inward/outward-open conformational cycles in SLC26A4 or effectively translated into lateral expansion for electromotility in SLC26A5. It is conceivable that the uncoupled fast channel-like anion transport by SLC26A9 may not require fully completed elevator-like motion cycles.

Attenuation of the inter-TM14 helices hydrophobic interaction induces hysteresis in SLC26A5 motor function

Mammalian SLC26A5 senses changes in transmembrane electric potentials (receptor potentials) and exerts electromotility, which is the molecular basis of cochlear amplification. It is likely that displacements of the core domains with respect to the gate domains (6, 7, 9, 32) are driven by voltage changes, and that NLC-inducing movements of a yet-to-be-fully identified voltage sensing charge(s) or dipole(s) are coupled to the

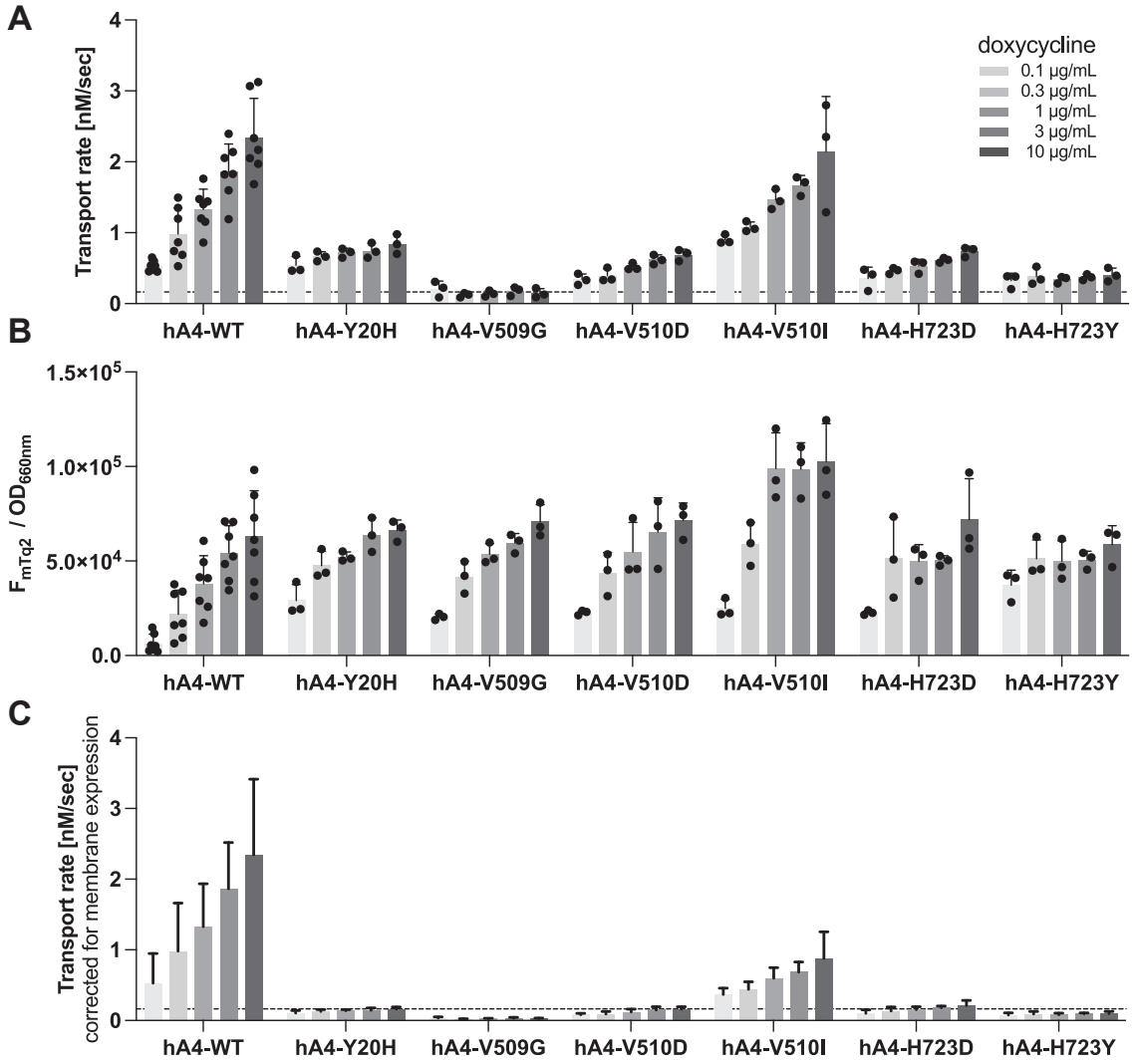

Figure 6. Multi-cell fluorometric bicarbonate/chloride antiport assays. *A*, bicarbonate/chloride antiport rates were measured in HEK293T cells expressing various SLC26A4 constructs in a Dox-dependent manner. A horizontal dashed line indicates the basal transport rate of non-induced cells (negative control). Error bars indicate standard deviation. *B*, ratios of mTq2 fluorescence (F_{mTq2}) and the optical densities (OD_{660nm}) of the cells expressing the mTq2-tagged SLC26A4 constructs, which quantify the total expressions of the SLC26A4 constructs. Error bars indicate standard deviation. *C*, SLC26A4-mediate bicarbonate/chloride antiport rates were corrected for the relative membrane expressions as in Fig. 4.

core domain displacements. As mentioned above, Val^{499} and Ile^{500} at the C-terminus of the TM14 helix hydrophobically interact with Val^{499} and Ile^{500} in the other TM14 helix in the homodimeric structure. We found that slight attenuation of this hydrophobic interaction by I500V did not affect NLC (see above). However, further attenuation of the hydrophobicity by I500A induces hysteresis in NLC measured by a sinusoidal voltage protocol (Fig. 7*A*) in mouse (Fig. 7*B*), gerbil (Fig. 7*C*), and naked mole-rat SLC26A5 (Fig. 7*D*). The observed NLC hysteresis might be explained by hyperpolarization- and depolarization-induced changes in the angle between the two TM14 helices, which would change the direction of the core domain displacements and concomitantly change the vector of the voltage-sensing charge movement. Thus, the emergence of NLC hysteresis supports the idea that SLC26A5's voltage sensor charge movement is tightly coupled to the relative displacements of the core domains with respect to the gate domains (Fig. 7*E*).

Other observations

A bicarbonate/chloride exchange activity in SLC26A9 is controversial (12, 25–28). Our SNARF-based fluorometric assay did not detect bicarbonate/chloride antiport activity in hA9-WT (Fig. S2). Therefore, what was measured in the whole-cell recording in Figure 3 would be an uncoupled chloride transport, although the solutions used were estimated to contain ∼150 μM HCO_3^- (under ∼400 ppm atmospheric CO_2 at pH 7.4). In our hands, we were not able to detect bicarbonate/chloride antiport activity in hA9-V393R either (Fig. S2), refuting the possibility that the V393R missense change may confer bicarbonate/chloride exchange function on SLC26A9.

Discussion

The homodimeric structures of SLC26A4, A5, A6, and A9 are strikingly similar. Given the high degree of amino acid

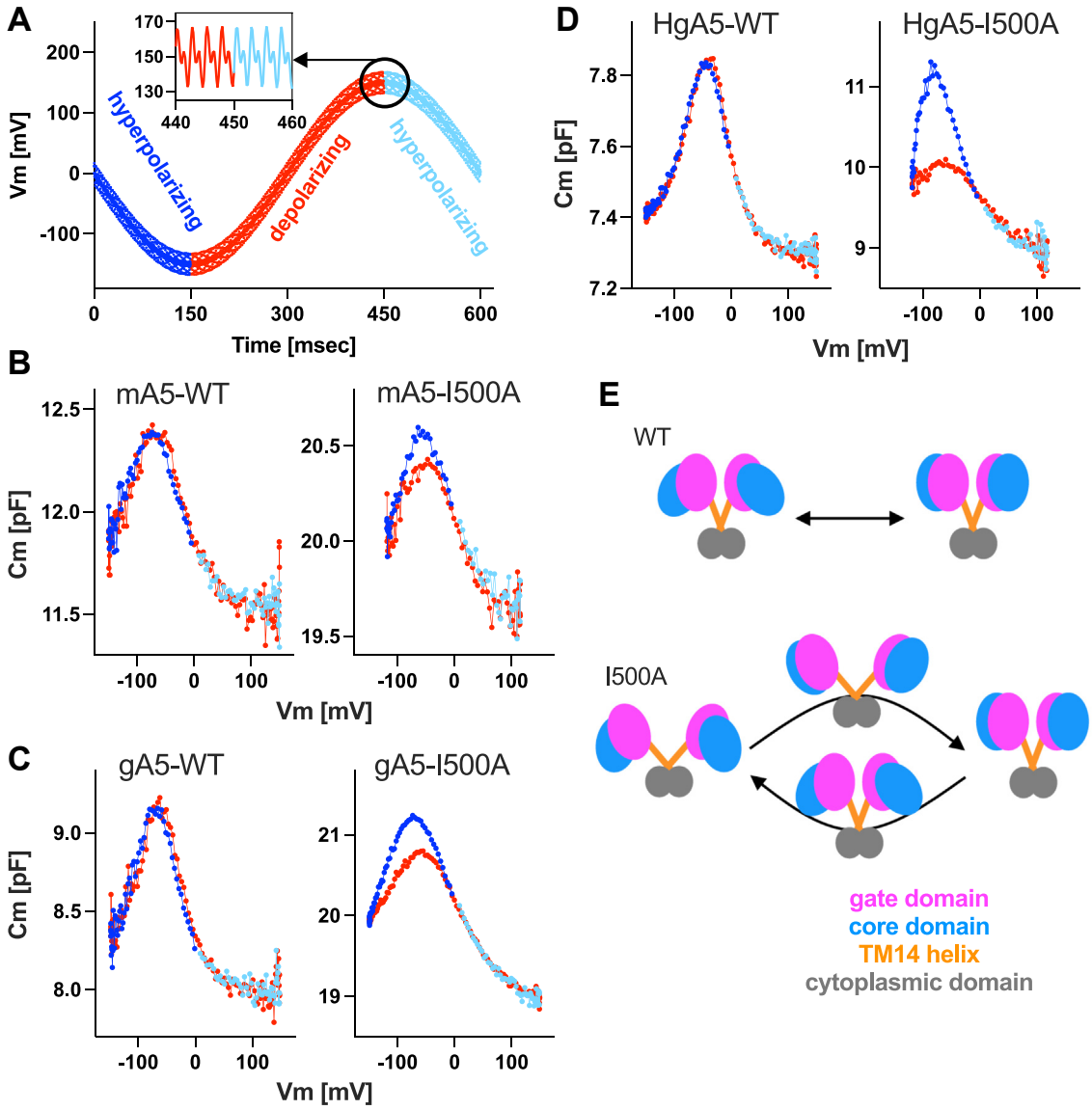

Figure 7. NLC hysteresis induced by I500A in SLC26A5. *A*, the voltage protocol used for whole-cell NLC recordings. An inset shows dual sinusoidal stimuli (390.6 and 781.2 Hz, 10 mV) superimposed onto a large sinusoidal voltage stimulus (with either 120 or 150 mV amplitude). *B–D*, NLC recorded in HEK293T cells expressing WT or I500A of a mouse (mA5, panel B), gerbil (gA5, panel C), and naked mole-rat (HgA5, panel D) SLC26A5. C_m values determined by hyperpolarizing and depolarizing voltage stimulus phases are indicated in different colors and matched with the color coding used in panel A. *E*, a hypothetical model to account for the observed NLC hysteresis (see the main text).

sequence similarity, it is probable that the other SLC26 family proteins also have similar homodimeric structures. Elevator-like motions of the core domains with respect to the gate domains intuitively account for the anion transport mechanism. In fact, inward- and outward-open conformations were experimentally captured for SLC26A4 (4). This gate/core relative motions can also account for the voltage-driven motor function of mammalian SLC26A5 (6, 7, 32), implying that the voltage-sensing mechanism in SLC26A5 may not be unique in the SLC26 family. In fact, SLC26A4 also exhibits a large NLC but with a shallow voltage sensitivity (small α) and extremely hyperpolarized V_{pk} (37). It is likely that movements of a voltage sensing charge(s) and/or dipole(s) are tightly coupled to the movements of the core domains, and that the efficiency of this electromechanical coupling is evolutionarily enhanced and optimized in mammalian SLC26A5. It is curious to learn if the loss of anion transport function is inevitable for optimizing the electromechanical coupling efficiency in mammalian SLC26A5. Comparative structural and functional studies on nonmammalian transporter SLC26A5 may address this outstanding question.

Whether the protomers functionally communicate in a homodimer complex is another outstanding question. The N- and C-termini are connected to the core and the gate domains, respectively, and interwound with one another at the bottom of the CD (Figs. 1 and S1). Previous studies demonstrated the importance of these N- and C-terminal regions for the function of SLC26A5 (67, 69). In SLC26A5, we presume that the N- and C-terminal interaction is important for stabilizing homodimerization, but not for inter-protomer communication, because

coexpression of a dysfunctional SLC26A5 (V499G/Y501H) did not affect the function of WT SLC26A5 upon heteromerization (68). Consistently, the present study found that Y16H and H707R barely affect NLC of SLC26A5 (Fig. 5). On the contrary, missense changes at equivalent sites in SLC26A9 (Y8H and H731R) and SLC26A4 (Y20H, H723D, H723Y) partially reduced or completely abrogated the anion transport functions, respectively (Figs. 3, 4, and 6). Based on these observations, we speculate that interprotomer functional interaction indeed exists in transporter SLC26 proteins and is particularly crucial for coupled anion transport such as bicarbonate/chloride exchange mediated by SLC26A4. The presence of many disease-associated *SLC26A4* missense variants that potentially affect the N- and C-terminal interaction is in line with such speculation.

We showed that V393R abolished the anion transport function of SLC26A9 (Figs. 3 and 4), but this single missense change did not confer NLC on SLC26A9 (Fig. 5). Likewise, R399V abolished NLC of SLC26A5 (Fig. 5), but it conferred only a very small chloride conductance on SLC26A5 (Fig. 3). It thus appears that the diverse functions of the SLC26 proteins are not attributable to a single or a few local amino acids change. Despite the overall structural similarity, the packing of the 14 TM helices differs among the SLC26 family of proteins (Fig. 1). The slightly denser packing of TM helices in mammalian SLC26A5 may be crucial for maximizing the electromechanical coupling efficiency and reducing the energy barrier between an expanded and a compacted states for attaining fast conformational transition kinetics (*i.e.*, fast electromotility). This speculative optimization may have resulted in loss of anion transport function during molecular evolution but may have been tolerated because the anion transport activity of SLC26A5 is of minimal physiological significance in mammalian hearing (24). Again, comparative structural and functional studies on nonmammalian transporter SLC26A5 may provide definitive mechanistic insights as to how the fast and efficient electromechanical coupling in mammalian SLC26A5 has evolved from ancestral anion transporters.

Although this study focused only on the SLC26 molecule itself for molecular mechanisms, other factors, that is, interacting proteins, also play roles to support their diverse physiological functions. For example, apical *versus* basolateral membrane localization of SLC26 proteins, which is probably dictated by yet-to-be-fully-defined distinct protein interactomes (70–72), is of obvious physiological significance but was not dealt in the present study using the nonpolarized cell line, HEK293T. Regulatory interactions are also possible (73–79) but not controlled, either, in the present study. It is likely that intrinsically disordered regions that were not resolved in the SLC26 structures reported to date are responsible for determining distinct membrane targeting and regulatory interactions, which need to be fully addressed in future studies. Nevertheless, the knowledge obtained by this comparative functional study would be useful in predicting the pathogenicity of variants found in this functionally diverse family of proteins.

Experimental procedures

Generation of stable cell lines that express various SLC26 protein constructs

cDNAs encoding human SLC26A4, mouse SLC26A5, gerbil SLC26A5, naked mole-rat SLC26A5, and human SLC26A9 (WT and missense mutants) with a C-terminally attached mTq2 tag were cloned into a pSBtet-pur vector (Addgene) using SfiI sites. Stable cell lines expressing these SLC26 constructs in a doxycycline-dependent manner were established in HEK293T cells as previously described (38). Stable cells were maintained in DMEM supplemented with 10% FBS and 1μg/ml puromycin (Fisher Scientific).

Whole-cell recordings

Whole-cell recordings were performed at room temperature using the Axopatch 200B amplifier (Molecular Devices) with a 10 kHz low-pass filter. Recording pipettes pulled from borosilicate glass were filled with an ionic-blocking intracellular solution containing (mM): 140 CsCl, 2 $MgCl_2$, 10 EGTA, and 10 HEPES (pH 7.4). L-aspartate was used to replace chloride for preparing low chloride-containing intracellular solutions. Cells were bathed in an extracellular solution containing (mM): 120 NaCl, 20 TEA-Cl, 2 $CoCl_2$, 2 $MgCl_2$, and 10 HEPES (pH 7.4). Osmolality was adjusted to 309 mOsmol/kg with glucose. Command voltages were step functions of 30 msec duration (from −100 mV to +100 mV or −50 mV to +50 mV, in 10 mV steps). Holding potentials were set to 0 mV. NLC was measured using sinusoidal voltage stimuli (2.5-Hz, 120 or 150 mV amplitude) superimposed with two higher frequency stimuli (390.6 and 781.2 Hz, 10 mV amplitude). Data were collected by jClamp (SciSoft Company, New Haven, CT) (80).

NLC data analysis

Voltage-dependent C_m data were analyzed using the following two-state Boltzmann equation:

$$C_m = \frac{\alpha Q_{max}\, exp\left[\alpha\left(V_m - V_{pk}\right)\right]}{\left\{1 + exp\left[\alpha\left(V_m - V_{pk}\right)\right]\right\}^2} + C_{lin} \qquad \text{(Eq. 1)}$$

where α is the slope factor of the voltage-dependence of charge transfer, Q_{max} is the maximum charge transfer, V_m is the membrane potential, V_{pk} is the voltage at which the maximum charge movement is attained, and C_{lin} is the linear capacitance. The specific capacitance, C_{sp}, was calculated as $(C_m - C_{lin})/C_{lin}$.

Fluorometric anion transport assay

Fluorometric HCO_3^-/Cl^- and I^-/Cl^- antiport assays were established and described in detail in a previous study (38). Briefly, stable HEK293T cells expressing SLC26 protein constructs or those with coexpressed iodide sensitive fluorescent protein, $mVenus^{H148Q/I152L}$, were used for HCO_3^-/Cl^- and I^-/Cl^- antiport assays, respectively. For the HCO_3^-/Cl^- antiport assay, cells were loaded with a pH indicator, SNARF-5F (S23923, Thermo Fisher Scientific) in a high chloride buffer containing

(mM): 140 NaCl, 4.5 KCl, 1 $MgCl_2$, 2.5 $CaCl_2$, 20 HEPES (pH 7.4). The antiport assay was initiated by an automated injection of a low chloride buffer containing (mM): 125 Na-gluconate, 5 K-gluconate, 1 $MgCl_2$, 1 $CaCl_2$, 20 HEPES, 25 $NaHCO_3$ with 5% CO_2 in Synergy Neo2 (Agilent/BioTek). For the I^-/Cl^- antiport assay, cells were resuspended in a high chloride buffer containing (mM): 150 NaCl, 1 $MgCl_2$, 1 $CaCl_2$, 20 HEPES (pH 7.5). The I^-/Cl^- antiport assay was initiated by an automated injection of a high iodide buffer containing (mM): 150 NaI, 1 $MgCl_2$, 1 $CaCl_2$, and 20 HEPES (pH 7.5). The fluorescence of SNARF-5F (for HCO_3^-/Cl^- antiport assay) or $mVenus^{H148Q/I152L}$ and mTq2 (for I^-/Cl^- antiport assay) were measured in a time-dependent manner using Synergy Neo2 (Agilent/BioTek) and the data analyzed offline as described previously (38).

Cell surface protein labeling and quantitation

Stable cells expressing SLC26 constructs were washed once with PBS, and 10 μM Sulfo-Cyanine3 NHS ester (Lumiprobe) dissolved in 2 ml of ice-cold PBS (per well of 6-well plate) was added and incubated for 30 min at 4 °C. The reaction was stopped by the addition of 200 μl of 100 mM glycine (per well). Cells were collected and lysed by sonication on ice in 500 μl of a lysis buffer containing 150 mM NaCl, 20 mM HEPES, pH 7.5, 1 mM EDTA, 20 mM DDM, 1 mM DTT, and 50 μg/ml leupeptin. The lysate was centrifuged at 16,000*g* for 5 minutes at 4 °C. A GFP selector slurry (5 μl, NanoTag Biotechnologies) was added to the supernatant and incubated for 30 minutes at 4 °C, with end-over-end mixing using a rotator. Bound proteins were collected alongside the GFP selector by brief centrifugation and observed with a fluorescent microscope (Leica DMIRB). Merged images of GFP selectors in cyan and red channels were analyzed using Fiji (81) to determine the fluorescent signal intensities of Cyanine3 (F_{Cy3}) and mTq2 (F_{mTq2}).

Propagated error calculation

Error propagations (σ) were calculated by the following equations:

$$\sigma_{AB} = |AB|\sqrt{\left(\frac{\sigma_A}{A}\right)^2+\left(\frac{\sigma_B}{B}\right)^2} \quad \text{(for multiplication)} \quad \text{(Eq. 2)}$$

$$\sigma_{A/B} = \left|\frac{A}{B}\right|\sqrt{\left(\frac{\sigma_A}{A}\right)^2+\left(\frac{\sigma_B}{B}\right)^2} \quad \text{(for division)} \quad \text{(Eq. 3)}$$

where A and B are the mean values with associated errors, σ_A and σ_B, respectively.

Statistical analyses

Statistical analyses were performed using Prism (GraphPad software). One-way ANOVA combined with Tukey's posttest was used for multiple comparisons. $p < 0.05$ was considered statistically significant. Kruskal-Wallis test with Dunn's post-test was also used for multiple comparisons in Figure 3*B*.

Nonlinear capacitance of SLC26A5 (prestin)

The voltage-driven motor activity of prestin and concurrent charge movement within the cell membrane (similar to gating currents in voltage-activated ion channels) are typically interpreted using a two-state model. This simple model assumes only two distinct voltage-dependent conformational states, S_1 and S_2 (Fig. S3*A*). The transition between the two states is governed by the two voltage-dependent rate constants, $k_{f(V)}$ and $k_{b(V)}$ (82). The mathematical expressions of these rates are as follows:

$$k_{f\,(v)} = k_{f(0)}\exp\left(\frac{zeV}{2k_BT}\right) \quad \text{(Eq. 4)}$$

$$k_{b(V)} = k_{b(0)}\exp\left(-\frac{zeV}{2k_BT}\right) \quad \text{(Eq. 5)}$$

where z, e, V, k_B, and T are the valence of charge movement, electron charge, the membrane electrical potential, the Boltzmann constant, and absolute temperature, respectively. $k_{f(0)}$ and $k_{b(0)}$ are rates of $k_{f(V)}$ and $k_{b(V)}$ at 0 mV. Using these rate constants, the equilibrium constant, K, is written as:

$$K = \frac{k_{f(v)}}{k_{b(v)}} = \frac{k_{f(0)}}{k_{b(0)}}\exp\left(\frac{zeV}{k_BT}\right) = \exp\left(\frac{zeV}{k_B\,T} - In\frac{k_{b(0)}}{k_{f(0)}}\right) = \exp\{\alpha(V-V_{pk})\} \quad \text{(Eq. 6)}$$

where

$$\alpha \equiv \frac{ze}{k_BT} \quad \text{(Eq. 7)}$$

$$V_{pk} \equiv \frac{k_BT}{ze}ln\frac{k_{b(0)}}{k_{f(0)}} = \alpha^{-1}\,ln\frac{k_{b(0)}}{k_{f(0)}} \quad \text{(Eq. 8)}$$

α is the slope factor of the voltage dependence of charge transfer, while V_{pk} is the voltage at which the maximum charge movement is attained. If N molecules of functional prestin are present, the number of molecules in the S_1 and S_2 states ($[S_1]$ and $[S_2]$, Fig. S3*B*) can be described as:

$$[S_1] = \frac{N}{1+K} \quad \text{(Eq. 9)}$$

$$[S_2] = \frac{NK}{1+K} \quad \text{(Eq. 10)}$$

Transition from S_1 to S_2 accompanies the movement of a voltage-sensing charge, ze. Therefore, the total charge moved,

Q, is computed as:

$$Q = ze[S_2] + C_{lin}V = \frac{zeNK}{1+K} + C_{lin}V = \frac{Q_{max}K}{1+K} + C_{lin}V \quad \text{(Eq. 11)}$$

where Q_{max} is the maximum charge transfer defined as zeN. In a whole-cell recording, membrane capacitive charge movement, $C_{lin}V$ (where C_{lin} is the membrane electric capacitance of a cell) also contributes to the overall charge movement (Fig. S3*C*). Differentiation of Equation 11 in terms of V yields voltage-dependent cell membrane capacitance (C_m):

$$C_m = \frac{dQ}{dV} = \frac{\alpha Q_{max}K}{(1+K)^2} + C_{\text{lin}} = \frac{\alpha Q_{max}\exp\{\alpha(V\text{-}V_{pk})\}}{(1+\exp\{\alpha(V\text{-}V_{\text{pk}})\})^2} + C_{lin} \quad \text{(Eq. 1)}$$

Thus, the expression of functional prestin confers bell-shaped C_m, referred to as nonlinear capacitance (NLC), on a host cell (Fig. S3*D*). The area between NLC and C_{lin} indicates Q_{max} (Fig. S3*D*). Currents associated with conformational transitions of prestin, I_p, is expressed as:

$$I_p = ze(k_{f(V)}[S_1] - k_{b(V)}[S_2]) \quad \text{(Eq. 12)}$$

Due to the nonlinearity in prestin's response to voltage, prestin-associated current induced by a ramped sinusoidal voltage stimulus also shows nonlinearity (Fig. S3*E*). Like cell membrane capacitive currents, prestin-associated current induced by a sinusoidal voltage stimulus is advanced by π/2 radians in phase with respect to an input sinusoidal voltage stimulus (Fig. S3*E*) if prestin's voltage-induced conformational transitions ($k_{f(V)} + k_{b(V)}$) are sufficiently fast as compared to the stimulus frequency. In principle, C_m can be determined from the phase-shifted currents elicited by a mono-sinusoidal voltage stimulus, as the capacitive admittance of the cell membrane depends only on C_m and the frequency of the voltage stimulus, f ($2\pi fC_m$). In reality, C_m determination is not that straightforward because contributions of the series (R_s) and the membrane (R_m) resistances to measured currents are often not negligible. To simultaneously determine all these whole-cell parameters (R_s, R_m, and C_m), we used the dual-sinusoidal method (83) that is implemented in jClamp (80).

Data availability

All data generated or analyzed during this study are included in this article. Raw numerical data will be made available upon request to the corresponding author.

Supporting information—This article contains supporting information.

Author contributions—K. H. conceptualization; K. H. methodology; K. H. and S. T. investigation; K. H. and S. T. formal analysis; K. H. and S. T. writing–original draft; K. H. funding acquisition.

Funding and additional information—This work was supported by an NIH grant DC017482 (to KH) and by the Hugh Knowles Center. The content is solely the responsibility of the authors and does not necessarily represent the official views of the National Institutes of Health.

Conflicts of interest—The authors declare that they have no known competing financial interests or personal relationships that could have appeared to influence the work reported in this paper.

Abbreviations—The abbreviations used are: CD, cytoplasmic domain; Dox, doxycycline; mTq2, mTurquoise2; SLC26, solute carrier 26; TM, transmembrane; TMD, transmembrane domain; WT, wild-type.

References

1. Alper, S. L., and Sharma, A. K. (2013) The SLC26 gene family of anion transporters and channels. *Mol. Aspects Med.* **34**, 494–515
2. Stenson, P. D., Mort, M., Ball, E. V., Chapman, M., Evans, K., Azevedo, L., *et al.* (2020) The Human Gene Mutation Database (HGMD((R))): optimizing its use in a clinical diagnostic or research setting. *Hum. Genet.* **139**, 1197–1207
3. Li, J., Huang, S., Liu, S., Liao, X., Yan, S., and Liu, Q. (2023) SLC26 family: a new insight for kidney stone disease. *Front. Physiol.* **14**, 1118342
4. Liu, Q., Zhang, X., Huang, H., Chen, Y., Wang, F., Hao, A., *et al.* (2023) Asymmetric pendrin homodimer reveals its molecular mechanism as anion exchanger. *Nat. Commun.* **14**, 3012
5. Wang, L., Hoang, A., Gil-Iturbe, E., Laganowsky, A., Quick, M., and Zhou, M. (2024) Mechanism of anion exchange and small-molecule inhibition of pendrin. *Nat. Commun.* **15**, 346
6. Ge, J., Elferich, J., Dehghani-Ghahnaviyeh, S., Zhao, Z., Meadows, M., von Gersdorff, H., *et al.* (2021) Molecular mechanism of prestin electromotive signal amplification. *Cell* **184**, 4669–4679.e4613
7. Bavi, N., Clark, M. D., Contreras, G. F., Shen, R., Reddy, B. G., Milewski, W., *et al.* (2021) The conformational cycle of prestin underlies outer-hair cell electromotility. *Nature* **600**, 553–558
8. Butan, C., Song, Q., Bai, J. P., Tan, W. J. T., Navaratnam, D., and Santos-Sacchi, J. (2022) Single particle cryo-EM structure of the outer hair cell motor protein prestin. *Nat. Commun.* **13**, 290
9. Futamata, H., Fukuda, M., Umeda, R., Yamashita, K., Tomita, A., Takahashi, S., *et al.* (2022) Cryo-EM structures of thermostabilized prestin provide mechanistic insights underlying outer hair cell electromotility. *Nat. Commun.* **13**, 6208
10. Tippett, D. N., Breen, C., Butler, S. J., Sawicka, M., and Dutzler, R. (2023) Structural and functional properties of the transporter SLC26A6 reveal mechanism of coupled anion exchange. *Elife* **12**, RP87178
11. Chi, X., Jin, X., Chen, Y., Lu, X., Tu, X., Li, X., *et al.* (2020) Structural insights into the gating mechanism of human SLC26A9 mediated by its C-terminal sequence. *Cell Discov.* **6**, 55
12. Walter, J. D., Sawicka, M., and Dutzler, R. (2019) Cryo-EM structures and functional characterization of murine Slc26a9 reveal mechanism of uncoupled chloride transport. *Elife* **8**, e46986
13. Choi, B. Y., Kim, H. M., Ito, T., Lee, K. Y., Li, X., Monahan, K., *et al.* (2011) Mouse model of enlarged vestibular aqueducts defines temporal requirement of Slc26a4 expression for hearing acquisition. *J. Clin. Invest.* **121**, 4516–4525
14. Everett, L. A., Belyantseva, I. A., Noben-Trauth, K., Cantos, R., Chen, A., Thakkar, S. I., *et al.* (2001) Targeted disruption of mouse Pds provides insight about the inner-ear defects encountered in Pendred syndrome. *Hum. Mol. Genet.* **10**, 153–161
15. Everett, L. A., Glaser, B., Beck, J. C., Idol, J. R., Buchs, A., Heyman, M., *et al.* (1997) Pendred syndrome is caused by mutations in a putative sulphate transporter gene (PDS). *Nat. Genet.* **17**, 411–422
16. Kim, H. M., and Wangemann, P. (2010) Failure of fluid absorption in the endolymphatic sac initiates cochlear enlargement that leads to deafness in mice lacking pendrin expression. *PLoS One* **5**, e14041

17. Li, X., Sanneman, J. D., Harbidge, D. G., Zhou, F., Ito, T., Nelson, R., *et al.* (2013) SLC26A4 targeted to the endolymphatic sac rescues hearing and balance in Slc26a4 mutant mice. *PLoS Genet.* **9**, e1003641
18. Zheng, J., Shen, W., He, D. Z., Long, K. B., Madison, L. D., and Dallos, P. (2000) Prestin is the motor protein of cochlear outer hair. *Cell Nat.* **405**, 149–155
19. Liberman, M. C., Gao, J., He, D. Z., Wu, X., Jia, S., and Zuo, J. (2002) Prestin is required for electromotility of the outer hair cell and for the cochlear amplifier. *Nature* **419**, 300–304
20. Wu, X., Gao, J., Guo, Y., and Zuo, J. (2004) Hearing threshold elevation precedes hair-cell loss in prestin knockout mice. *Brain Res. Mol. Brain Res.* **126**, 30–37
21. Cheatham, M. A., Huynh, K. H., Gao, J., Zuo, J., and Dallos, P. (2004) Cochlear function in Prestin knockout mice. *J. Physiol.* **560**, 821–830
22. Dallos, P., Wu, X., Cheatham, M. A., Gao, J., Zheng, J., Anderson, C. T., *et al.* (2008) Prestin-based outer hair cell motility is necessary for mammalian cochlear amplification. *Neuron* **58**, 333–339
23. Mistrík, P., Daudet, N., Morandell, K., and Ashmore, J. F. (2012) Mammalian prestin is a weak Cl(-)/HCO(3)(-) electrogenic antiporter. *J. Physiol.* **590**, 5597–5610
24. Takahashi, S., Zhou, Y., Kojima, T., Cheatham, M. A., and Homma, K. (2023) Prestin's fast motor kinetics is essential for mammalian cochlear amplification. *Proc. Natl. Acad. Sci. U. S. A.* **120**, e2217891120
25. Xu, J., Henriksnas, J., Barone, S., Witte, D., Shull, G. E., Forte, J. G., *et al.* (2005) SLC26A9 is expressed in gastric surface epithelial cells, mediates Cl-/HCO3- exchange, and is inhibited by NH4+. *Am. J. Physiol. Cell Physiol.* **289**, C493–C505
26. Dorwart, M. R., Shcheynikov, N., Wang, Y., Stippec, S., and Muallem, S. (2007) SLC26A9 is a Cl(-) channel regulated by the WNK kinases. *J. Physiol.* **584**, 333–345
27. Loriol, C., Dulong, S., Avella, M., Gabillat, N., Boulukos, K., Borgese, F., *et al.* (2008) Characterization of SLC26A9, facilitation of Cl(-) transport by bicarbonate. *Cell Physiol. Biochem.* **22**, 15–30
28. Chang, M. H., Plata, C., Zandi-Nejad, K., Sindic, A., Sussman, C. R., Mercado, A., *et al.* (2009) Slc26a9–anion exchanger, channel and Na+ transporter. *J. Membr. Biol.* **228**, 125–140
29. Xu, J., Song, P., Miller, M. L., Borgese, F., Barone, S., Riederer, B., *et al.* (2008) Deletion of the chloride transporter Slc26a9 causes loss of tubulovesicles in parietal cells and impairs acid secretion in the stomach. *Proc. Natl. Acad. Sci. U. S. A.* **105**, 17955–17960
30. Anagnostopoulou, P., Riederer, B., Duerr, J., Michel, S., Binia, A., Agrawal, R., *et al.* (2012) SLC26A9-mediated chloride secretion prevents mucus obstruction in airway inflammation. *J. Clin. Invest.* **122**, 3629–3634
31. Amlal, H., Xu, J., Barone, S., Zahedi, K., and Soleimani, M. (2013) The chloride channel/transporter Slc26a9 regulates the systemic arterial pressure and renal chloride excretion. *J. Mol. Med. (Berl)* **91**, 561–572
32. Kuwabara, M. F., Haddad, B. G., Lenz-Schwab, D., Hartmann, J., Longo, P., Huckschlag, B. M., *et al.* (2023) Elevator-like movements of prestin mediate outer hair cell electromotility. *Nat. Commun.* **14**, 7145
33. Zhao, J., Yuan, Y., Huang, S., Huang, B., Cheng, J., Kang, D., *et al.* (2014) KCNJ10 may not be a contributor to nonsyndromic enlargement of vestibular aqueduct (NSEVA) in Chinese subjects. *PLoS One* **9**, e108134
34. Jang, J. H., Jung, J., Kim, A. R., Cho, Y. M., Kim, M. Y., Lee, S. Y., *et al.* (2014) Identification of novel functional null allele of SLC26A4 associated with enlarged vestibular aqueduct and its possible implication. *Audiol. Neurootol.* **19**, 319–326
35. Dai, P., Yuan, Y., Huang, D., Zhu, X., Yu, F., Kang, D., *et al.* (2008) Molecular etiology of hearing impairment in Inner Mongolia: mutations in SLC26A4 gene and relevant phenotype analysis. *J. Transl Med.* **6**, 74
36. Miyagawa, M., Nishio, S. Y., Usami, S., and Deafness Gene Study, C. (2014) Mutation spectrum and genotype-phenotype correlation of hearing loss patients caused by SLC26A4 mutations in the Japanese: a large cohort study. *J. Hum. Genet.* **59**, 262–268
37. Kuwabara, M. F., Wasano, K., Takahashi, S., Bodner, J., Komori, T., Uemura, S., *et al.* (2018) The extracellular loop of pendrin and prestin modulates their voltage-sensing property. *J. Biol. Chem.* **293**, 9970–9980
38. Wasano, K., Takahashi, S., Rosenberg, S. K., Kojima, T., Mutai, H., Matsunaga, T., *et al.* (2020) Systematic quantification of the anion transport function of pendrin (SLC26A4) and its disease-associated variants. *Hum. Mutat.* **41**, 316–331
39. Chen, D. Y., Chen, X. W., Jin, X., Zuo, J., Wei, C. G., Cao, K. L., *et al.* (2007) [Screening of SLC26A4 (PDS) gene mutation in cochlear implant recipients with inner ear malformation]. *Zhonghua Yi Xue Za Zhi* **87**, 2820–2824
40. Van Hauwe, P., Everett, L. A., Coucke, P., Scott, D. A., Kraft, M. L., Ris-Stalpers, C., *et al.* (1998) Two frequent missense mutations in Pendred syndrome. *Hum. Mol. Genet.* **7**, 1099–1104
41. Chai, Y., Huang, Z., Tao, Z., Li, X., Li, L., Li, Y., *et al.* (2013) Molecular etiology of hearing impairment associated with nonsyndromic enlarged vestibular aqueduct in East China. *Am. J. Med. Genet. A* **161A**, 2226–2233
42. Park, H. J., Shaukat, S., Liu, X. Z., Hahn, S. H., Naz, S., Ghosh, M., *et al.* (2003) Origins and frequencies of SLC26A4 (PDS) mutations in east and south Asians: global implications for the epidemiology of deafness. *J. Med. Genet.* **40**, 242–248
43. Yuan, Y., Guo, W., Tang, J., Zhang, G., Wang, G., Han, M., *et al.* (2012) Molecular epidemiology and functional assessment of novel allelic variants of SLC26A4 in non-syndromic hearing loss patients with enlarged vestibular aqueduct in China. *PLoS One* **7**, e49984
44. Gillam, M. P., Bartolone, L., Kopp, P., and Benvenga, S. (2005) Molecular analysis of the PDS gene in a nonconsanguineous Sicilian family with Pendred's syndrome. *Thyroid* **15**, 734–741
45. Dossena, S., Rodighiero, S., Vezzoli, V., Nofziger, C., Salvioni, E., Boccazzi, M., *et al.* (2009) Functional characterization of wild-type and mutated pendrin (SLC26A4), the anion transporter involved in Pendred syndrome. *J. Mol. Endocrinol.* **43**, 93–103
46. Zhang, C. R., Shi, Y. P., Zhang, C. X., Sun, F., Zhu, W. J., Zhang, R. J., *et al.* (2022) Mutation screening and functional study of SLC26A4 in Chinese patients with congenital hypothyroidism. *J. Clin. Res. Pediatr. Endocrinol.* **14**, 46–55
47. Takahashi, S., Kojima, T., Wasano, K., and Homma, K. (2024) Functional studies of deafness-associated pendrin and prestin variants. *Int. J. Mol. Sci.* **25**, 2759
48. Oliver, D., He, D. Z., Klöcker, N., Ludwig, J., Schulte, U., Waldegger, S., *et al.* (2001) Intracellular anions as the voltage sensor of prestin, the outer hair cell motor protein. *Science* **292**, 2340–2343
49. Santos-Sacchi, J., Song, L., Zheng, J., and Nuttall, A. L. (2006) Control of mammalian cochlear amplification by chloride anions. *J. Neurosci.* **26**, 3992–3998
50. Santos-Sacchi, J., and Tan, W. (2022) On the frequency response of prestin charge movement in membrane patches. *Biophys. J.* **121**, 2371–2379
51. Bai, J. P., Surguchev, A., Montoya, S., Aronson, P. S., Santos-Sacchi, J., and Navaratnam, D. (2009) Prestin's anion transport and voltage-sensing capabilities are independent. *Biophys. J.* **96**, 3179–3186
52. Gorbunov, D., Sturlese, M., Nies, F., Kluge, M., Bellanda, M., Battistutta, R., *et al.* (2014) Molecular architecture and the structural basis for anion interaction in prestin and SLC26 transporters. *Nat. Commun.* **5**, 3622
53. Yoon, J. S., Park, H. J., Yoo, S. Y., Namkung, W., Jo, M. J., Koo, S. K., *et al.* (2008) Heterogeneity in the processing defect of SLC26A4 mutants. *J. Med. Genet.* **45**, 411–419
54. Ishihara, K., Okuyama, S., Kumano, S., Iida, K., Hamana, H., Murakoshi, M., *et al.* (2010) Salicylate restores transport function and anion exchanger activity of missense pendrin mutations. *Hear Res.* **270**, 110–118
55. Lee, H. J., Jung, J., Shin, J. W., Song, M. H., Kim, S. H., Lee, J. H., *et al.* (2014) Correlation between genotype and phenotype in patients with bi-allelic SLC26A4 mutations. *Clin. Genet.* **86**, 270–275
56. Jung, J., Kim, J., Roh, S. H., Jun, I., Sampson, R. D., Gee, H. Y., *et al.* (2016) The HSP70 co-chaperone DNAJC14 targets misfolded pendrin for unconventional protein secretion. *Nat. Commun.* **7**, 11386
57. Prasad, S., Kolln, K. A., Cucci, R. A., Trembath, R. C., Van Camp, G., and Smith, R. J. (2004) Pendred syndrome and DFNB4-mutation screening of SLC26A4 by denaturing high-performance liquid chromatography and

the identification of eleven novel mutations. *Am. J. Med. Genet. A* **124A**, 1–9
58. Anwar, S., Riazuddin, S., Ahmed, Z. M., Tasneem, S., Ateeq ul, J., Khan, S. Y., *et al.* (2009) SLC26A4 mutation spectrum associated with DFNB4 deafness and Pendred's syndrome in Pakistanis. *J. Hum. Genet.* **54**, 266–270
59. Coyle, B., Reardon, W., Herbrick, J. A., Tsui, L. C., Gausden, E., Lee, J., *et al.* (1998) Molecular analysis of the PDS gene in Pendred syndrome. *Hum. Mol. Genet.* **7**, 1105–1112
60. Pryor, S. P., Madeo, A. C., Reynolds, J. C., Sarlis, N. J., Arnos, K. S., Nance, W. E., *et al.* (2005) SLC26A4/PDS genotype-phenotype correlation in hearing loss with enlargement of the vestibular aqueduct (EVA): evidence that Pendred syndrome and non-syndromic EVA are distinct clinical and genetic entities. *J. Med. Genet.* **42**, 159–165
61. Tian, Y., Xu, H., Liu, D., Zhang, J., Yang, Z., Zhang, S., *et al.* (2021) Increased diagnosis of enlarged vestibular aqueduct by multiplex PCR enrichment and next-generation sequencing of the SLC26A4 gene. *Mol. Genet. Genomic Med.* **9**, e1734
62. Usami, S., Abe, S., Weston, M. D., Shinkawa, H., Van Camp, G., and Kimberling, W. J. (1999) Non-syndromic hearing loss associated with enlarged vestibular aqueduct is caused by PDS mutations. *Hum. Genet.* **104**, 188–192
63. Blons, H., Feldmann, D., Duval, V., Messaz, O., Denoyelle, F., Loundon, N., *et al.* (2004) Screening of SLC26A4 (PDS) gene in Pendred's syndrome: a large spectrum of mutations in France and phenotypic heterogeneity. *Clin. Genet.* **66**, 333–340
64. Rendtorff, N. D., Schrijver, I., Lodahl, M., Rodriguez-Paris, J., Johnsen, T., Hansen, E. C., *et al.* (2013) SLC26A4 mutation frequency and spectrum in 109 Danish Pendred syndrome/DFNB4 probands and a report of nine novel mutations. *Clin. Genet.* **84**, 388–391
65. Choi, B. Y., Stewart, A. K., Madeo, A. C., Pryor, S. P., Lenhard, S., Kittles, R., *et al.* (2009) Hypo-functional SLC26A4 variants associated with nonsyndromic hearing loss and enlargement of the vestibular aqueduct: genotype-phenotype correlation or coincidental polymorphisms? *Hum. Mutat.* **30**, 599–608
66. Pera, A., Dossena, S., Rodighiero, S., Gandia, M., Botta, G., Meyer, G., *et al.* (2008) Functional assessment of allelic variants in the SLC26A4 gene involved in Pendred syndrome and nonsyndromic EVA. *Proc. Natl. Acad. Sci. U. S. A.* **105**, 18608–18613
67. Zheng, J., Du, G. G., Matsuda, K., Orem, A., Aguiñaga, S., Deák, L., *et al.* (2005) The C-terminus of prestin influences nonlinear capacitance and plasma membrane targeting. *J. Cell Sci.* **118**, 2987–2996
68. Homma, K., Duan, C., Zheng, J., Cheatham, M. A., and Dallos, P. (2013) The V499G/Y501H mutation impairs fast motor kinetics of prestin and has significance for defining functional independence of individual prestin subunits. *J. Biol. Chem.* **288**, 2452–2463
69. Navaratnam, D., Bai, J. P., Samaranayake, H., and Santos-Sacchi, J. (2005) N-terminal-mediated homomultimerization of prestin, the outer hair cell motor protein. *Biophys. J.* **89**, 3345–3352
70. Sengupta, S., Miller, K. K., Homma, K., Edge, R., Cheatham, M. A., Dallos, P., *et al.* (2010) Interaction between the motor protein prestin and the transporter protein VAPA. *Biochim. Biophys. Acta* **1803**, 796–804
71. Cimerman, J., Waldhaus, J., Harasztosi, C., Duncker, S. V., Dettling, J., Heidrych, P., *et al.* (2013) Generation of somatic electromechanical force by outer hair cells may be influenced by prestin-CASK interaction at the basal junction with the Deiter's cell. *Histochem. Cell Biol.* **140**, 119–135
72. Li, M., Nishio, S. Y., Naruse, C., Riddell, M., Sapski, S., Katsuno, T., *et al.* (2020) Digenic inheritance of mutations in EPHA2 and SLC26A4 in Pendred syndrome. *Nat. Commun.* **11**, 1343
73. Ko, S. B., Zeng, W., Dorwart, M. R., Luo, X., Kim, K. H., Millen, L., *et al.* (2004) Gating of CFTR by the STAS domain of SLC26 transporters. *Nat. Cell Biol.* **6**, 343–350
74. Chang, M. H., Plata, C., Sindic, A., Ranatunga, W. K., Chen, A. P., Zandi-Nejad, K., *et al.* (2009) Slc26a9 is inhibited by the R-region of the cystic fibrosis transmembrane conductance regulator via the STAS domain. *J. Biol. Chem.* **284**, 28306–28318
75. Bai, J. P., Surguchev, A., Ogando, Y., Song, L., Bian, S., Santos-Sacchi, J., *et al.* (2010) Prestin surface expression and activity are augmented by interaction with MAP1S, a microtubule-associated protein. *J. Biol. Chem.* **285**, 20834–20843
76. Homma, K., Miller, K. K., Anderson, C. T., Sengupta, S., Du, G. G., Aguiñaga, S., *et al.* (2010) Interaction between CFTR and prestin (SLC26A5). *Biochim. Biophys. Acta* **1798**, 1029–1040
77. Ohana, E., Shcheynikov, N., Moe, O. W., and Muallem, S. (2013) SLC26A6 and NaDC-1 transporters interact to regulate oxalate and citrate homeostasis. *J. Am. Soc. Nephrol.* **24**, 1617–1626
78. Keller, J. P., Homma, K., Duan, C., Zheng, J., Cheatham, M. A., and Dallos, P. (2014) Functional regulation of the SLC26-family protein prestin by calcium/calmodulin. *J. Neurosci.* **34**, 1325–1332
79. Xu, J., Barone, S., Varasteh Kia, M., Holliday, L. S., Zahedi, K., and Soleimani, M. (2022) Identification of IQGAP1 as a SLC26A4 (Pendrin)-Binding protein in the kidney. *Front. Mol. Biosci.* **9**, 874186
80. Santos-Sacchi, J., Kakehata, S., and Takahashi, S. (1998) Effects of membrane potential on the voltage dependence of motility-related charge in outer hair cells of the Guinea-pig. *J. Physiol.* **510**(Pt 1), 225–235
81. Schindelin, J., Arganda-Carreras, I., Frise, E., Kaynig, V., Longair, M., Pietzsch, T., *et al.* (2012) Fiji: an open-source platform for biological-image analysis. *Nat. Methods* **9**, 676–682
82. Hille, B. (1984) *Ionic Channels of Excitable Membranes*, Sinauer Associates, Sunderland, Mass
83. Pusch, M., and Neher, E. (1988) Rates of diffusional exchange between small cells and a measuring patch pipette. *Pflugers Arch.* **411**, 204–211